Journal of Marine Research, 61, 577–611, 2003

The Pacific/Indian Ocean pressure difference and its influence on the Indonesian Seas circulation: Part I—The study with specified total transports

by William H. Burnett[1], Vladimir M. Kamenkovich[2], Arnold L. Gordon[3] and George L. Mellor[4]

ABSTRACT

The main objective of this paper is to investigate the overall balance of momentum and energy within the Indonesian Seas to better understand the factors that control the total transport of the Indonesian Throughflow. Two models are used in the investigation: a "first-step" heuristic channel model and a more sophisticated "second-step," barotropic numerical model that incorporates high-resolution coastline and bottom topography. The experiments show that the barotropic model develops typical horizontal circulation patterns for the region. An analysis of the overall momentum and energy balances suggests that the total transport of the Indonesian Throughflow does not depend exclusively on the inter-ocean pressure difference but on other factors, including local winds, bottom form stresses, and the resultant of pressure forces acting on the internal sides.

1. Introduction

Due to Wyrtki's (1961) efforts, and others, we know that basically three currents supply water to the Indonesian Seas: the Mindanao Current, the New Guinea Coastal Current, and the New Guinea Coastal Undercurrent (see e.g. Fine *et al.,* 1994 and references given therein). In the Northern Hemisphere, the North Equatorial Current splits at approximately 14N as it encounters the Philippines and separates into the northward-flowing Kuroshio and the southward-flowing Mindanao Current (see e.g. Gordon, 1986). The Mindanao Current splits into three branches: two branches flow into the Celebes Sea and the Molucca Sea, while the third branch curves to join the North Equatorial Countercurrent (see e.g. Kashino *et al.,* 2001). The New Guinea Coastal Undercurrent flows along the eastern New Guinea coast and splits between the Halmahera Sea and the North Equatorial Countercurrent, while the New Guinea Coastal Current fluctuates from a northerly to a southerly

---

[1] Naval Meteorology and Oceanography Command, Stennis Space Center, Mississippi, 39529-5001, U.S.A. ***email: burnettb@cnmoc.navy.mil***

[2] Department of Marine Science, The University of Southern Mississippi, Stennis Space Center, Mississippi, 39529, U.S.A.

[3] Lamont Doherty Earth Observatory of Columbia University, Palisades, New York, 10964, U.S.A.

[4] Program in Atmospheric and Oceanic Sciences, Princeton University, Princeton, New Jersey, 08544, U.S.A.

current depending upon the monsoon winds (see e.g. Murray *et al.,* 1995). Water from the Celebes Sea flows south into the Makassar Strait and splits between the Lombok Strait and the Flores Sea (see e.g. Gordon, 2001), while waters from the Molucca Sea flow into the Banda Sea and recombine with the Makassar Strait flow. Indonesian Seas waters exit through three regions: the Lombok Strait (see e.g. Murray and Arief, 1988), the Ombai Strait and the Timor Sea (see e.g. Potemra *et al.,* 2002). The set of all the individual currents flowing through the Indonesian Seas is labeled as one current called the Indonesian Throughflow (ITF).

Wyrtki (1987) hypothesized that the transport of water from the Pacific to the Indian Ocean is driven by the pressure gradient between the two oceans and used the observed sea level difference at Davao, Philippines and Darwin, Australia along with the appropriate hydrographic data to analyze the variations of the ITF transport. Is this hypothesis justified dynamically? There are some interesting papers devoted to the study of the influence of the inter-ocean pressure gradient on the Indonesian Seas circulation (Godfrey, 1996; Godfrey and Masumoto, 1999; Nof, 1995a,b; 1996, and references given therein). Nevertheless we think that the question—"How much does the Pacific-Indian Ocean pressure difference influence the ITF?"—has not yet been clarified sufficiently and therefore requires further analysis.

In Part I we will first describe a "first-step" heuristic model that is useful in formulating some important dynamical questions. Further we will outline a "second-step" barotropic numerical model to take into account the Indonesian Seas bottom relief and coastline. A comparison of the circulation patterns and transports, with and without a local wind stress, will be made to observations and other modeling studies to estimate the relevancy of the model. The central point of the paper is to analyze the overall balance of momentum and energy aimed at developing a better understanding of factors that control the total transport of the Indonesian Throughflow.

2. The "first-step" model

In his pioneering paper Wyrtki (1961) applied a simple channel model to analyze the relation between the pressure gradient and the transport in some Indonesian Seas passages. In this section we will use the same approach and consider large-scale barotropic motions in a meridional channel as a heuristic model of the circulation in the region. The main idea of the approach is borrowed from studies of pipe dynamics where the pressure difference between two sections of a pipe (the pressure head) drives the flow. It is customary to use the overall momentum and energy equations for only a section of the pipe to determine the relation between the pressure head, the total transport of the flow, and the along-channel component of the resultant of the pressure forces acting on the walls of the pipe (see, e.g., Lighthill, 1996; Section 1). Note that the resultant of pressure forces acting on the walls of the pipe is analogous to the bottom form stress in ocean dynamics.

Consider a channel with solid boundaries at $x = 0$ and $x = X$ and the open boundaries at $y = 0$ and $y = Y$. Suppose that this region lies outside the equator and can be viewed as part of some larger region. We assume that the pressure and velocity at $y = Y$ are formed by some external factors acting outside the region. Such an approach is typical for a regional model. Our objective is to show that, generally speaking, the pressure gradient along the channel does not uniquely determine the total transport of the channel flow, Q.

We will use Munk's (1950) model. The corresponding equations and boundary conditions are:

$$-fS_y = -gH\frac{\partial\eta}{\partial x} + A\Delta S_x + \tau_x, \tag{1}$$

$$fS_x = -gH\frac{\partial\eta}{\partial y} + A\Delta S_y + \tau_y, \tag{2}$$

$$\frac{\partial S_x}{\partial x} + \frac{\partial S_y}{\partial y} = 0, \tag{3}$$

$$S_x = 0; \qquad S_y = 0; \qquad \text{at } x = 0, x = X, \tag{4}$$

where the x-axis is directed eastward, the y-axis is directed northward; $\mathbf{S} = (S_x, S_y)$ is the transport velocity (depth integrated vector of horizontal velocity); η is the sea-surface height; f is the Coriolis parameter; g is the acceleration of gravity; A is the coefficient of horizontal turbulent viscosity; H is the depth of the channel; $\boldsymbol{\tau} = (\tau_x, \tau_y)$ is the wind stress divided by ρ_0 (the mean density); and Δ is the 2D Laplace operator. Boundary conditions in the y-direction will be discussed later.

We will consider several hypothetical types of motion to demonstrate the possibility of different relationships between the total transport of the channel flow, Q, and the pressure gradient along the channel. The friction coefficient A is assumed to be small, so in the interior region (outside the possible boundary layers) we have:

$$-fS_y^{(i)} = -gH\frac{\partial\eta^{(i)}}{\partial x} + \tau_x, \tag{5}$$

$$fS_x^{(i)} = -gH\frac{\partial\eta^{(i)}}{\partial y} + \tau_y, \tag{6}$$

$$\frac{\partial S_x^{(i)}}{\partial x} + \frac{\partial S_y^{(i)}}{\partial y} = 0, \tag{7}$$

where the superscript i refers to the interior.

Cross-differentiating (5) and (6) and using (7) yields:

$$\mathbf{S}^{(i)} \cdot \nabla\left(\frac{f}{H}\right) = \text{curl}_z\left(\frac{\boldsymbol{\tau}}{H}\right). \tag{8}$$

The potential vorticity in the interior is equal to f/H. Hence the component of $\mathbf{S}^{(i)}$ perpendicular to the pv-isoline is found. We specify the direction of the pv-isolines by turning the vector $\boldsymbol{\nabla}(f/H)$ by 90° in the counterclockwise direction. It is well known that the component of $\mathbf{S}^{(i)}$ along the pv-isoline can be obtained by integrating $\boldsymbol{\nabla} \cdot \mathbf{S}^{(i)} = 0$ along the pv-isoline in the positive direction, starting with some specified values at the boundary (boundary condition). Note that directions of pv-isolines determine the location of the boundary layers.

Case 1: $H =$ const. The pattern will consist of the interior and Munk's boundary layer motions. In the boundary layer we have:

$$-fS_y^{(b)} = -gH\frac{\partial \eta^{(b)}}{\partial x}, \tag{9}$$

$$fS_x^{(b)} = -gH\frac{\partial \eta^{(b)}}{\partial y} + A\frac{\partial^2 S_y^{(b)}}{\partial x^2} + \tau_y(0, y), \tag{10}$$

$$\frac{\partial S_x^{(b)}}{\partial x} + \frac{\partial S_y^{(b)}}{\partial y} = 0 \tag{11}$$

where the superscript b refers to the boundary layer. From (9)–(11) we derive

$$\beta S_y^{(b)} = A\frac{\partial^3 S_y^{(b)}}{\partial x^3}; \qquad \beta = \frac{\partial f}{\partial y}. \tag{12}$$

We will consider the boundary-layer solution to this equation which satisfies the condition $S_y^{(b)} = 0$ at $x = 0$:

$$S_y^{(b)} = \frac{2}{\sqrt{3}}\frac{Q^{(b)}(y)}{L_m}\exp\left(-\frac{x}{2L_m}\right)\sin\left(\frac{\sqrt{3}}{2}\frac{x}{L_m}\right); \qquad L_m = \left(\frac{A}{\beta}\right)^{1/3} \tag{13}$$

where the total transport of the boundary current $Q^{(b)}(y)$ is to be specified. Stommel and Arons (1960) used a similar approach by allowing the formation of part of a boundary-layer transport outside the region under study.

Assume $\boldsymbol{\tau} = 0$. Then $S_x^{(i)} = 0$; $S_y^{(i)} = 0$ and all the motion is concentrated in the boundary layer. In this case $Q^{(b)} =$ const and $S_x^{(b)} = 0$. Therefore (10) reduces to

$$0 = -gH\frac{\partial \eta^{(b)}}{\partial y} + A\frac{\partial^2 S_y^{(b)}}{\partial x^2}. \tag{14}$$

Integrating (14) across the boundary layer and using (13) gives:

$$-gH\frac{\partial}{\partial y}\left(\int_0^\infty \eta^{(b)}dx\right) = \beta L_m Q^{(b)}. \tag{15}$$

Thus, although $S_y^{(b)}$ is determined according to (9) by the pressure gradient across the channel, the total transport $Q^{(b)}$ appears uniquely related to the pressure gradient along the channel (integrated over the depth and across the boundary layer). It is interesting to compare this result with the similar result for the so-called "geostrophically controlled" flow valid for some time range of the nonstationary motion (Toulany and Garrett, 1984; Pratt, 1991). In principle, we can interpret Eq. (15) in the following ways: (1) the prescribed pressure difference along the channel drives the channel flow or (2) the prescribed $Q^{(b)}$ creates the pressure difference along the channel. The former is preferable because qualitatively it is rather clear how the actual pressure difference between the Pacific and Indian Ocean is created.

We will now incorporate the wind stress. From (7) and (8) we find:

$$S_y^{(i)} = \frac{1}{\beta}\,\mathrm{curl}_z\,\boldsymbol{\tau}; \qquad S_x^{(i)} = \frac{1}{\beta}\int_x^X \frac{\partial}{\partial y}(\mathrm{curl}_z\,\boldsymbol{\tau})dx. \tag{16}$$

Integrating (11) across the boundary layer (from 0 to ∞) yields:

$$Q^{(b)}(y) = Q^{(b)}(Y) + \int_y^Y S_x^{(i)}(0, y)dy. \tag{17}$$

So $Q^{(b)}(Y)$ can be considered as an arbitrarily prescribed value. Note that the total transport of the channel flow, Q, is determined as

$$Q = \int_0^X S_y^{(i)}dx + Q^{(b)}(y). \tag{18}$$

Due to condition (4), the total transport, Q, is constant.

Now we will take the relation for the sea-surface height, η,

$$\eta(x, y) = \eta^{(i)}(x, y) + \eta^{(b)}(x, y) - \eta^{(i)}(0, y). \tag{19}$$

and integrate (6), across the region (from 0 to X), and (10), across the boundary layer (from 0 to ∞). Invoking (11), (13), (16), and (18) yields, after some manipulations:

$$-gH\frac{\partial}{\partial y}\left(\int_0^X \eta dx\right) = \int_0^X \left[\frac{f}{\beta}(x - L_m)\frac{\partial}{\partial y}(\mathrm{curl}_z\,\boldsymbol{\tau}) - L_m\,\mathrm{curl}_z\,\boldsymbol{\tau} - \tau_y\right]dx + \beta L_m Q. \tag{20}$$

We see that not only the pressure gradient along the channel determines the total transport Q of the channel flow, but the local wind stress as well.

It is interesting to note that from (10) and (12) we readily obtain that

$$-gH\frac{\partial \eta^{(b)}}{\partial y}\bigg|_{x=0} = \beta Q^{(b)}(y) - \tau_y(0, y). \tag{21}$$

Estimating τ_y as $10^{-4}\,\mathrm{m}^2\,\mathrm{s}^{-2}$, we see that both terms on the right-hand side of (21) are on the same order.

Godfrey (1996; Fig. 3) demonstrated an interesting application of this formula (neglecting $\tau_y(0, y)$). He calculated the depth integrated pressure gradient from Irian Jaya to the south by specifying the total transport of the ITF. Integrating this gradient from the equator to 10S made it possible to estimate the values of depth integrated steric height that appeared in an excellent agreement with observations.

Note, however, that if we calculate the along-channel pressure gradient at the eastern coast, we obtain

$$-gH\frac{\partial \eta^{(i)}}{\partial y}\bigg|_{x=X} = -\tau_y(X, y). \tag{22}$$

Case 2: $H \neq$ const. It is clear that in the case of variable H, the bottom form stress can modify these balances. To emphasize this important point we will consider an extreme case of *free* meridional flow. For such a flow the pressure gradient along the channel is equal to zero. Due to the dependence of H on y, the area of the cross-section will depend also on y. So the resultant of the pressure forces acting on the sides $y = 0$ and $y = Y$ (the pressure head) will not be equal to zero and will be balanced by the resultant of pressure forces acting on the bottom (the bottom form stress). Thus a motion is possible when there is no relation at all between the total transport Q and the pressure gradient along the channel.

The following is a quantitative analysis of this case. Traditionally the analysis of the boundary layer is based on the vorticity equation. We will continue, however, to put more emphasis on the analysis of the momentum equations within the boundary layer. Veronis (1981; pp. 150–151) was among the first to stress the usefulness of such an approach.

A free meridional flow should go along pv-isolines. Therefore we choose a very special H such that:

$$\frac{\partial}{\partial x}\left(\frac{f}{H}\right) < 0; \qquad \frac{\partial}{\partial y}\left(\frac{f}{H}\right) = 0, \tag{23}$$

for which pv-isolines are straight lines parallel to boundaries $x = 0$ and $x = X$. Such H exists: $H(x, y) = A(x)\exp(\beta y)$, where $A(x)$ has positive derivative.

Suppose that $\boldsymbol{\tau} = 0$. Then according to (5)–(7); and (4), free meridional flow is possible:

$$S_x^{(i)} = 0; \qquad S_y^{(i)} = S_y^{(i)}(x); \qquad \eta^{(i)} = \eta^{(i)}(x), \tag{24}$$

where $S_y^{(i)}(x)$ is arbitrarily prescribed at $y = Y$. Assume that there is no southern boundary layer at $y = 0$. Consider the following general formula:

$$\int_0^X\int_0^Y gH\,\frac{\partial\eta^{(i)}}{\partial y}\,dxdy = \int_0^X [g\eta^{(i)}H(x,\,Y) - g\eta^{(i)}H(x,\,0)]dx - \int_0^X\int_0^Y g\eta^{(i)}\,\frac{\partial H}{\partial y}\,dxdy, \tag{25}$$

valid for any $\eta^{(i)}$ and H. We can interpret (25) so that the volume integral of the pressure gradient can be represented as the difference of the pressure head (the first term on the right-hand side of (25)) and the bottom form stress (the second term on the same side of (25); see Appendix B). For a free flow, the left-hand side of (25) is zero, so the pressure head is balanced by the bottom form stress:

$$\int_0^X [g\eta^{(i)}H(x,\,Y) - g\eta^{(i)}H(x,\,0)]dx = \int_0^X\int_0^Y g\eta^{(i)}\,\frac{\partial H}{\partial y}\,dxdy. \tag{26}$$

It is important to note that in this case the total transport of the channel flow, Q, is formed by some external factors lying beyond the model considered and has no relation to the pressure head within the region.

Notice that (15), (20) and (26) are just the overall momentum equations along the channel. The overall energy equation gives the same formulas (15) and (20) but degenerates in Case 2. We also note that in this section we have considered only those boundary layers that influence the total transport Q.

Thus we have examined three dynamically consistent flows:

1. The total transport of the channel flow, Q, is uniquely connected with the pressure gradient *along* the channel (H = const; $\boldsymbol{\tau} = 0$).
2. The total transport of the channel flow, Q, depends not only on the pressure gradient *along* the channel but on the local wind stress as well (H = const; $\boldsymbol{\tau} \neq 0$).
3. The total transport of the channel flow, Q, is not influenced by the pressure head within the region at all. The bottom form stress balances completely the action of pressure head ($H(x, y) = A(x)\exp(\beta y)$; $\boldsymbol{\tau} = 0$).

It is supposed that in all three cases at least part of the total transport of the channel flow, Q, is formed outside the considered region.

3. The second-step model

The heuristic first-step model suggests that the relation between the inter-ocean pressure difference and the total transport Q is influenced by the bottom relief and local winds. How does this result apply to the Indonesian Seas where the coastline and bathymetry are extremely complicated? We will use a numerical model to further investigate this relationship. For our initial efforts we will use a high-resolution, regional, barotropic model based on the Princeton Ocean Model (Blumberg and Mellor, 1987; Mellor, 1999). Short descriptions of our preliminary results were published in Burnett and Kamenkovich (1999) and Burnett *et al.* (2000a,b).

There are several reasons for using a barotropic model. First of all, the overall problem is very complicated and moving from the first-step model to a high-resolution baroclinic model may cause us to miss some important factors that govern the throughflow. For example, it is reasonable to start formulating the appropriate open boundary conditions with a barotropic model. We will also show that the consideration of the barotropic model will allow us to develop relevant tools for the analysis of the overall momentum and energy balances. These tools will also be critical for the analysis of the baroclinic experiments. It is known that the baroclinic component of the circulation is strong, especially in the Makassar Strait. Based on this fact several authors, e.g. Kindle *et al.* (1987; 1989); Godfrey (1989; 1996); Inoue and Welsh (1993); Wajsowicz (1993a,b; 1994; 1999); Nof (1995a,b; 1996); Qiu *et al.* (1999), have successfully applied the so-called reduced-gravity model to the analysis of the Indonesian Seas circulation. The effect of the bottom topography was basically ignored in these models although some attempts to estimate it have been performed (Wajsowicz, 1993a; Godfrey, 1996; Godfrey and Masumoto, 1999). But the existence of a pronounced baroclinic component does not imply that weaker near-bottom currents can be neglected.

The impact of the bottom topography on the circulation depends on near-bottom velocities and we have strong evidence that the bottom topography actually influences the Indonesian Seas circulation (see e.g. Gordon and McLean, 1999). An analysis of Lebedev and Yaremchuk's (2000) diagnostic calculations indicate that the near-bottom velocities are on the same order as barotropic ones. The root mean square (rms) errors for the zonal and meridional near-bottom velocities are 2.6 and 2.7 cm s^{-1}, respectively, while the rms for the corresponding barotropic velocities are 1.9 and 2.6 cm s^{-1}. Also, the usual objection to barotropic flow has to do with how the topography affects the direction of the flow but in our case the channels and passages will 'lead' the flow so this effect is mitigated (see Section 5). Therefore, we will use the barotropic model to acquire a preliminary understanding of the influence of bottom topography on the circulation.

The goal is not to reproduce all the features of the Indonesian Seas circulation as close to reality as possible, but to analyze the role of some physical factors that control the circulation. Our model, like any regional model, will use some open boundary conditions to replicate the flow of water from the Pacific Ocean to the Indian Ocean, and these boundary conditions will impose certain limitations on the interpretation of our results. For example, we cannot reveal the external factors responsible for the formation of total transport or the pressure difference between the Pacific and Indian Ocean. We would need a global numerical model to perform a complete analysis of all the external factors that influence the ITF. However, a global model still requires enormous computational resources to perform numerical experiments with relevant horizontal resolutions. Moreover to study the influence of some factors we usually need a series of such experiments. At the same time we can easily perform high-resolution experiments with a regional model. It is worth stressing that, with existing computer resources, the horizontal resolution of the regional model can be sufficiently high to adequately incorporate the complicated bottom topography and coastline of the Indonesian Seas. It will be demonstrated that the regional model can estimate the *relation* between the total transport of the ITF, on the one hand, and the inter-ocean pressure difference, the bottom form stress, the local wind stress, and the resultant of pressure forces acting on the internal walls, on the other hand.

4. An overview of model specifics

Figure 1 illustrates the rectangular model domain rotated to align the western boundary of the model with oceanographic survey sections obtained during the Java Australia Dynamic Experiment (JADE) survey program. The four open ports simulate the major ocean currents that influence the ITF: the Mindanao Current (MC) inflow, the North Equatorial Counter Current (NECC) outflow, the New Guinea Coastal Current (NGCC) inflow, and the Indian Ocean (IO) outflow.

Our model will use a Mercator map projection with a curvilinear orthogonal coordinate system (x, y) applied to the model domain. This coordinate system is automatically generated by the Princeton Ocean Model (POM), however, the spherical geometry is insignificant in the area. The center of the coordinate system is located at the southwest corner of the domain. At the southern boundary, $0 \leq x \leq X$ and $y = 0$; on the western boundary $x = 0$ and $0 \leq y \leq Y$. The model bathymetry was taken from the ETOPO5 database at 1/12° resolution (Fig. 2). The depth integrated continuity equation and the horizontal momentum equations used in this study are described in the POM User's Guide (Mellor, 1999) while some specifics regarding the difference formulation of the basic equations and the initial/boundary conditions are described in Appendix A. We will use a coefficient of horizontal friction, $A = 500\ \mathrm{m}^2\,\mathrm{s}^{-1}$; however, some experiments are performed with $A = 50\ \mathrm{m}^2\,\mathrm{s}^{-1}$ to analyze the sensitivity of the model. Normal and tangential velocities are set to zero at all the boundaries except at the four open ports. All experiments are initialized with horizontal velocities and sea-surface heights set to zero throughout the model domain and are ramped during the first 30 computational days to reduce the impact of transient motion.

For this study, seasonal descriptions are made relative to the Northern Hemisphere, with the seasonally prescribed transports through the four open ports taken from historical and simulated data. The MC seasonal inflow transport, Q_{MC}, is derived from Miyama *et al.* (1995), who provided an estimate of the MC volume transport across 8N. The IO seasonal outflow transport, Q_{IO}, is derived from Fieux *et al.* (1996) by integrating the total transport across the East Gyral Current and the South Equatorial Current during the spring and fall, and then interpolating the transports for winter and summer. The NGCC seasonal inflow transport, Q_{NGCC}, is derived from Murray *et al.* (1995) observations of transport through the Vitiaz Strait for March (winter) and August (summer) 1992, assuming the transport

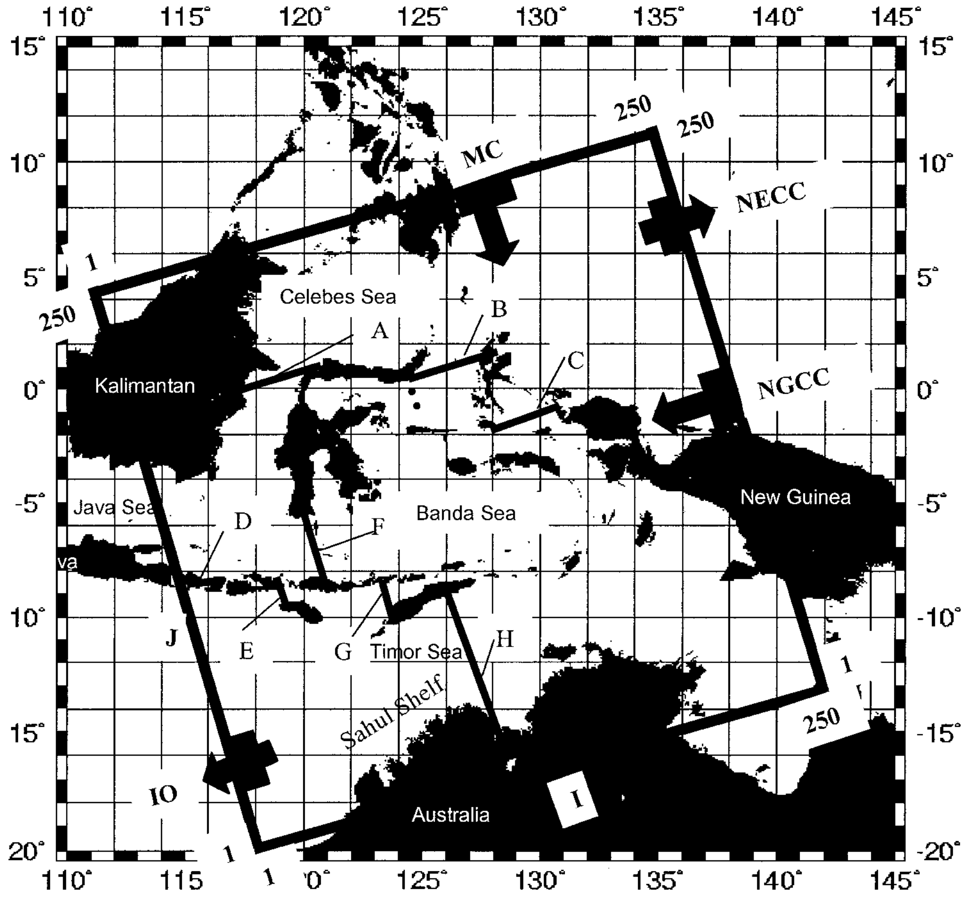

Figure 1. Map of the Indonesian Seas area with the model domain outlined by the black box. The domain corner coordinates are: Southwest (20S, 118E); Northwest (4N, 111E); Northeast (11N, 135E); Southeast (13S, 142E). The location of the model four open ports are denoted by black-filled rectangle boxes with labels indicating the name of the port: Mindanao Current (MC) inflow, North Equatorial Counter Current (NECC) outflow, New Guinea Coastal Current (NGCC) inflow, and Indian Ocean (IO) outflow. Arrows indicate the direction of the port flow. The location of the domain grid cells are denoted by I and J. Solid lines denote the passageways used to measure the throughflow and are identified by letters A–H (see Table A.2).

through the Strait is representative of the NGCC total transport, and interpolating the values for spring and fall. The NECC seasonal outflow transport, Q_{NECC}, balances the total inflow and outflow through the other open ports to ensure volume conservation with the model domain. The outflow transports are considered positive (Q_{IO}, Q_{NECC}), while the inflow transports as negative (Q_{NGCC}, Q_{MC}), see Table A.1. Therefore:

$$Q_{\mathrm{IO}} + Q_{\mathrm{NGCC}} + Q_{\mathrm{NECC}} + Q_{\mathrm{MC}} = 0. \tag{27}$$

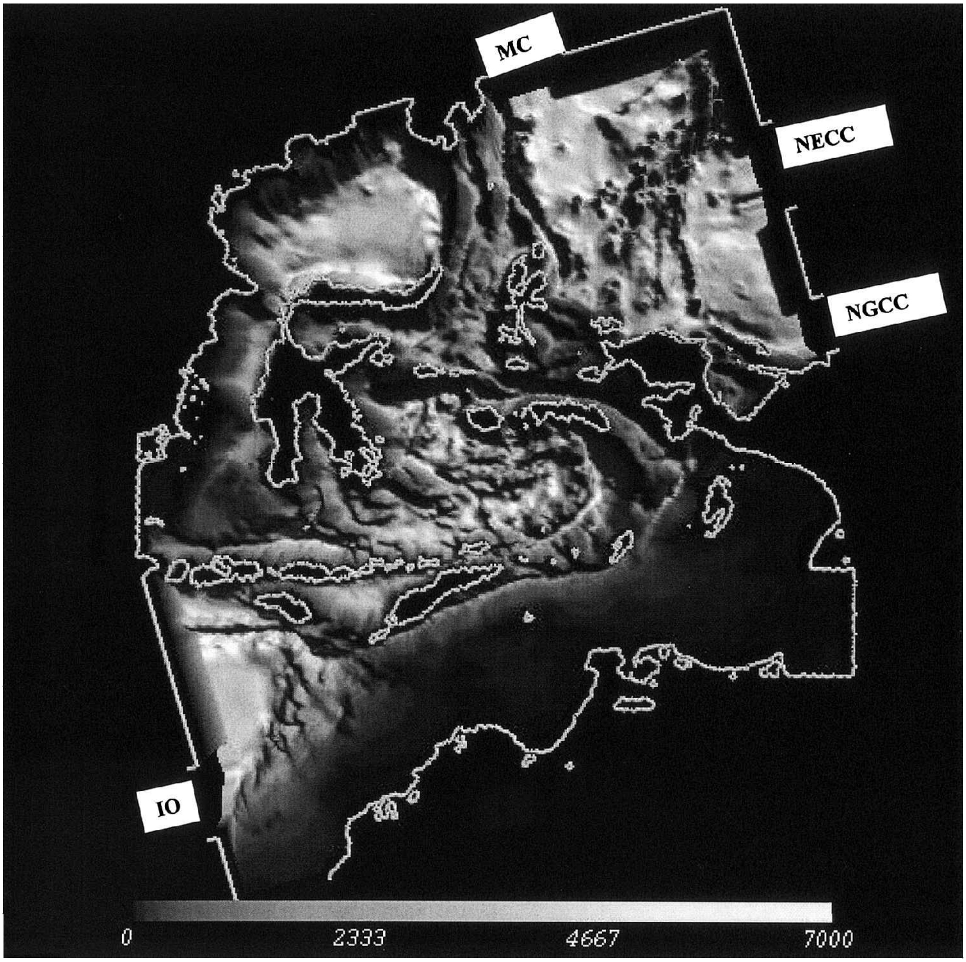

Figure 2. Model bathymetry of the Indonesian Seas region. The gray scale below the plot relates to the isobaths in meters. The locations of the open ports are labeled by the port abbreviations.

By specifying the transports we assume that the impact of the specific distribution of the velocity within the port rapidly decays at some distance from the port. In other words, by putting the ports far from the region of primary interest, we assume that only the values of these transports matter. Although the values of the transports are specified by using available observational and simulated data, certain mismatches between these values and the values determined by the large-scale interaction of the Indonesian Seas and the Pacific and Indian Ocean are unavoidable. This is, however, a general problem inherent in any regional model. Note that, even though the transports are prescribed at the open ports, the transport through the model straits and seas are determined by the internal dynamics of the model.

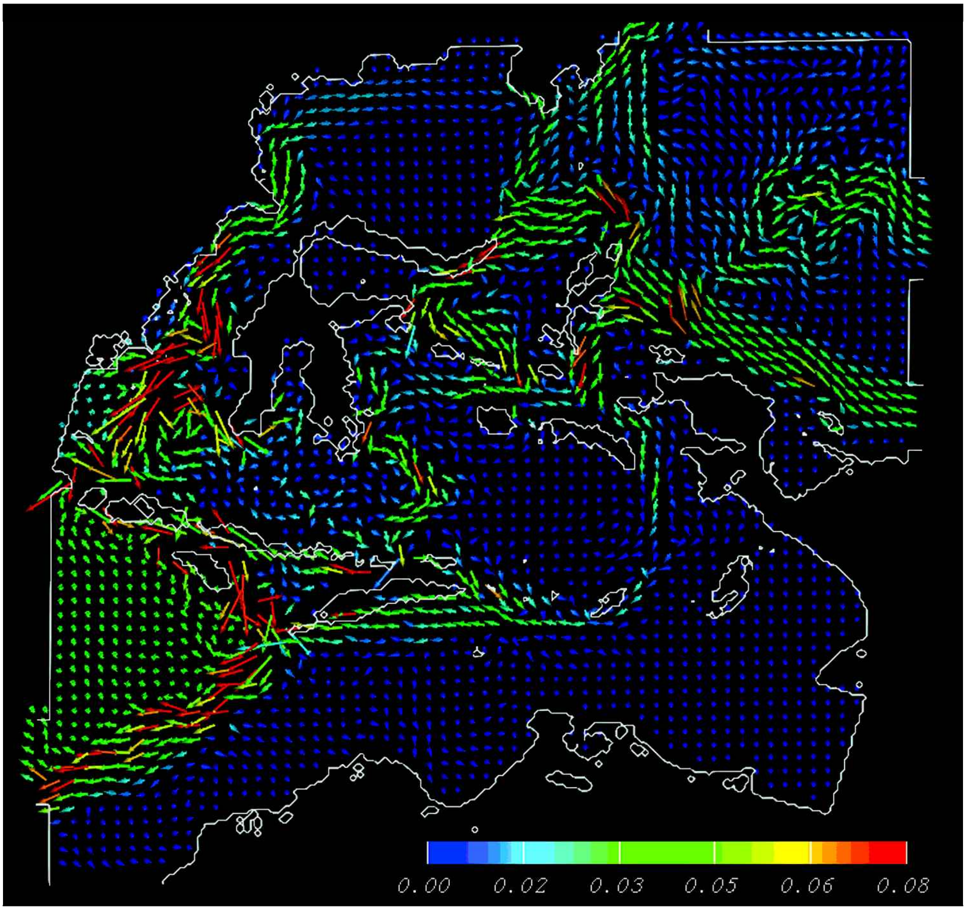

Figure 3. The horizontal velocity pattern ($A = 500 \text{ m}^2 \text{ s}^{-1}$) in m s^{-1} for the boreal summer without local wind forcing.

5. Circulation patterns

The numerical model produces circulation patterns that are generally consistent with observations and other numerical model results. Figure 3 presents the boreal summer horizontal velocity patterns over the entire model domain without local wind forcing. The MC splits between the Celebes Sea, the Molucca Sea, and the NECC (Lukas *et al.,* 1996; Godfrey, 1996; Gordon and Fine, 1996). The model did not develop a closed cyclonic gyre (the Mindanao Eddy) or a closed anticyclonic gyre (the Halmahera Eddy) as depicted by Fine *et al.* (1994) but the general features of the two-gyre system can be seen in Figure 3. The cyclonic flow around the Celebes Sea is a prominent feature in the model with most, if not all, the Celebes Sea circulation entering the Makassar Strait. When a wind stress is applied to the model, simulating the southeast monsoon (Fig. 4), the flow into the NECC

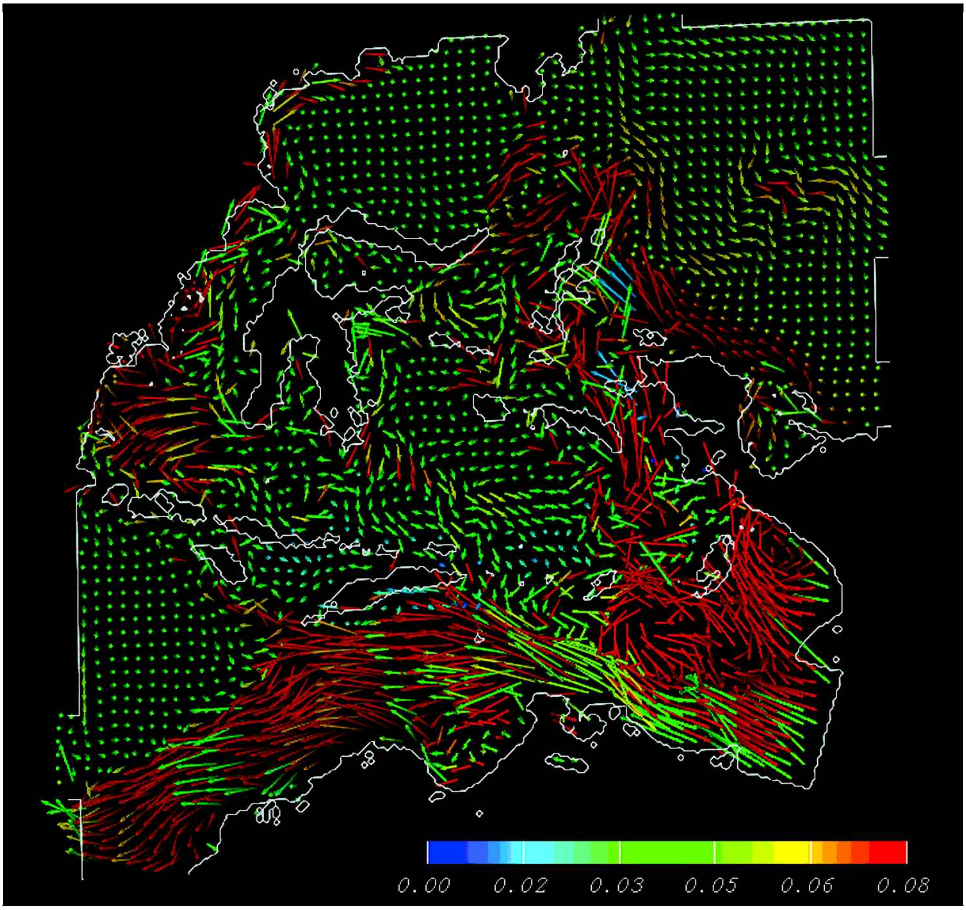

Figure 4. The horizontal velocity pattern (m s^{-1}) for the boreal summer with local wind forcing included.

increases while the transport into the Celebes Sea is less, since the wind induces an Ekman transport to the right of the MC. Additionally, the Makassar Strait transport is significantly less during the southeast monsoon. Table 1 presents the transports calculated through the eight selected passageways with and without local wind forcing. The locations selected are similar to those chosen by Potemra *et al.* (1997).

The majority of the ITF is through the Molucca Sea, instead of the Makassar Strait (Fig. 5a). This agrees with the model results from Potemra *et al.* (1997). However, the result is different from observations (Fine, 1985; Ffield and Gordon, 1992; Gordon and Fine, 1996) that show the Makassar Strait as the primary pathway from the Pacific to the Indian Ocean. Baroclinic models, both prognostic and diagnostic, (Metzger and Hurlburt, 1996; Wajsowicz, 1999; Lebedev and Yaremchuk, 2000) with sufficient horizontal

Table 1. Absolute values of the total transports for the boreal summer (southeast monsoon season) calculated at the entrance of the four ports and eight passages; with and without local wind forcing ($A = 500$ m^2 s^{-1}). The letters next to the names of the passageways are used to identify the locations of the passageway cross-sections (see Fig. 1).

Passage	Without wind (Sv)	With wind (Sv)
Indian Ocean (outflow) or ITF	20.00	20.00
New Guinea Coastal Current (inflow)	19.00	19.00
North Equatorial Countercurrent (outflow)	25.00	25.00
Mindanao Current (inflow)	26.00	26.00
Makassar Strait (A)	6.44	2.78
Molucca Sea (B)	10.87	10.52
Halmahera Sea (C)	3.10	5.81
Lombok Strait (D)	4.50	1.11
Sumba Strait (E)	3.58	0.89
Flores Sea (F)	0.87	1.86
Ombai Strait (G)	9.35	4.46
Timor Sea (H)	5.08	14.75

resolution to resolve the Indonesian Seas passageways show the majority of the ITF passing through the upper 500 m of the Makassar Strait. While the physics that controls the splitting of the North Pacific inflow between the Makassar Strait and the Molucca Sea are not well understood, it is possible that the vertical structure of the Indonesian Seas circulation is an important factor that controls the splitting.

Figure 5b shows the NGCC splitting between the Halmahera Sea, the Molucca Sea, and the NECC, a pattern similar to the pattern defined by Gordon and Fine (1996). During the southeast monsoon, the wind stress is almost parallel to the NGCC. This induces a strong Ekman flow along the coast of New Guinea, which increases the transport into the Halmahera. The southeast monsoon actually strengthens the transport into the Halmahera Sea since Ekman transport is to the left of the wind stress in the southern hemisphere, and the Halmahera transport is slightly perpendicular to the wind stress.

The majority of the Makassar Strait flow (Fig. 5c) follows the deep open channel similar to observations by Gordon *et al.* (1999) and splits between the Lombok Strait and the Flores Sea (Fine *et al.,* 1994; Gordon and Fine, 1996). This flow is less during the southeast monsoon since transport through the Celebes Sea is smaller. In the Molucca Sea, the throughflow travels along the western boundary, around a number of islands within the basin, and flows into the Banda Sea. During the southeast monsoon, the MC splitting did not affect the amount of transport that entered the Molucca Sea since a significant amount of water was detoured from the Celebes Sea into the Molucca Sea.

The ITF can take a number of different pathways to exit the Indonesian Seas. The majority of the Makassar Strait flow in the model travels through the Lombok Strait instead of the Flores Sea—approximately 3 to 1, respectively. Fine *et al.* (1994) and Arief and Murray (1996) observed the opposite—with ¾ of the mean flow traveling through the

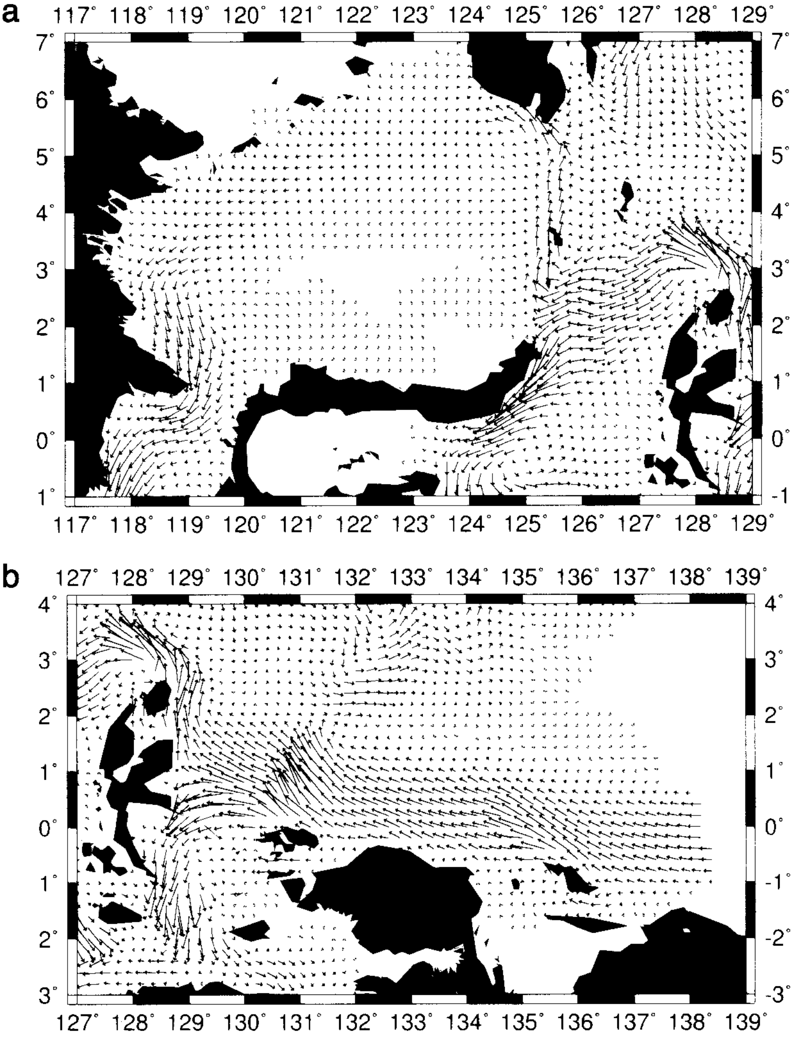

Figure 5. Horizontal velocity patterns ($A = 500$ m^2 s^{-1}) in the Celebes and Molucca Seas (a), the Halmahera Sea (b), Makassar and Lombok Strait (c), and the Ombai Strait and Timor Sea (d) for the boreal summer without local wind forcing.

Flores Sea and ¼ through the Lombok Strait. In experiments where A is set to 50 m^2 s^{-1}, or where the bottom topography is set to a constant value of 4500 m, we found that the flow actually increases through the Lombok Strait. However, during the southeast monsoon the transport significantly decreases through the Lombok and increases through the Flores Sea. Therefore, it seems that the baroclinicity of the flow and wind stress are important factors controlling the splitting in the area. Once the Flores Sea water recombines with the Molucca Sea and the Halmahera Sea flow in the Banda Sea, a portion of the Flores Sea flow

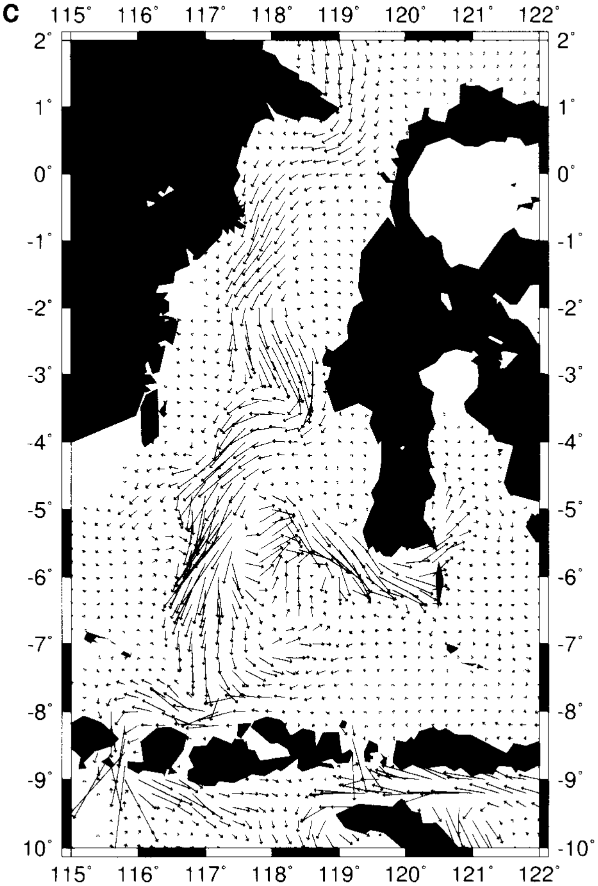

Figure 5. (Continued)

travels south through the Sumba Strait while the rest travels through the Ombai Strait, similar to Potemra *et al.* (1997). The remaining ITF outflow turns toward the Timor Sea (Fig. 5d) and combines with the flow from the Banda Sea, shoulders the Sahul Shelf, and exits through the IO. During the southeast monsoon the flow through the Timor Sea is significantly higher compared to the other straits.

The model is able to replicate the inter-ocean pressure difference between the Pacific and Indian Ocean (Fig. 6) where the sea-surface height, η, is higher in the Pacific domain compared to η in the Indian Ocean. We will focus on what extent this pressure difference influences the total transport of the ITF in the next section.

6. The momentum and energy balances

Initially we will neglect the local wind forcing; however, this effect will be discussed later in the paper. A comparison between the horizontal pressure gradient and the Coriolis

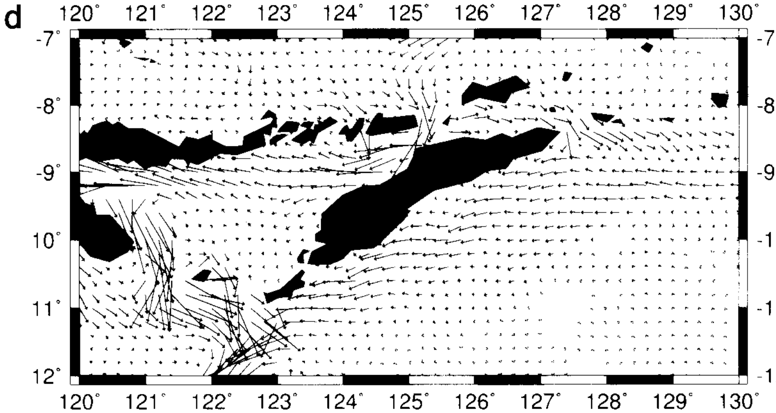

Figure 5. (Continued)

acceleration was described in Burnett *et al.* (2000a) and Burnett (2000). It was shown that the geostrophic approximation is, in general, applicable at the four open ports, except the southern edge of the IO port and the southern and northern edges of the NGCC open port. Moreover, for all seasons, the geostrophic approximation holds over a majority of the model domain. There are some observations confirming this result for time-averaged velocities (see, e.g. Chong *et al.,* 2000; Potemra *et al.,* 2002). Of course, the geostrophic approximation is not applicable along the equator and within some narrow and shallow parts of the area.

To better understand the dynamical processes that influence and determine the ITF, an analysis of the integral momentum and energy balances is produced. Multiplying the x-momentum equation by D and integrating it over the model domain, S, gives the overall x-momentum balance:

$$\frac{\partial}{\partial t}\int_S UDdS + \int_S \left\{ \frac{1}{m_x m_y}\left[\frac{\partial}{\partial x}(m_y UDU) + \frac{\partial}{\partial y}(m_x VDU) \right] - CVD \right\} dS$$
$$- \underbrace{\int_S fVDdS}_{\text{XCOR}} = - \underbrace{\int_S \frac{gD}{m_x}\frac{\partial \eta}{\partial x} dS}_{\text{XPGRD}} + \int_S \{DF_x - \tau_x^{(b)}\} dS, \tag{28}$$

$$C = \frac{1}{m_x m_y}\left(V\frac{\partial m_y}{\partial x} - U\frac{\partial m_x}{\partial y} \right); \tag{29}$$

m_x and m_y are metric scale factors along the x and y coordinate lines; $D = H + \eta$ is the total depth of the ocean, η is the sea-surface height and H is the depth; U and V are the depth averaged x and y components of horizontal velocity respectively (U; $V = (1/D) \int_{-H}^{\eta} (u; v)dz$); f is the Coriolis parameter; g is the gravitational acceleration; F_x and F_y are

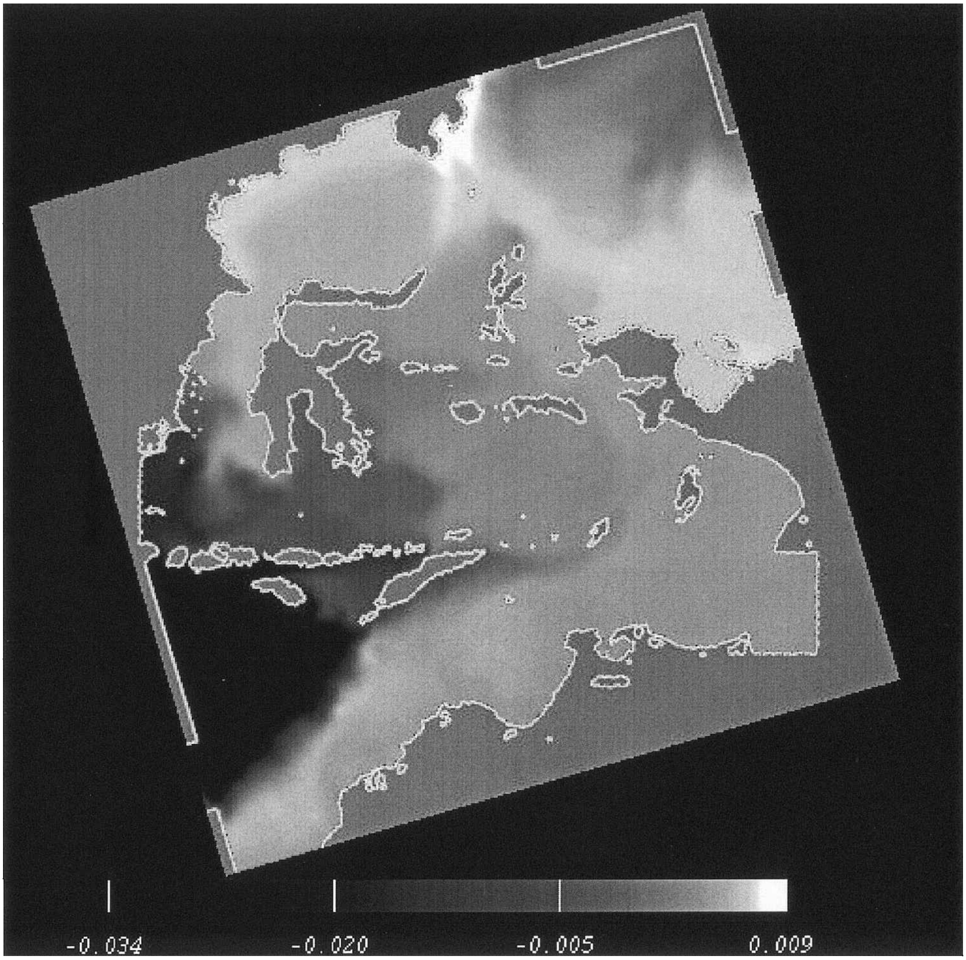

Figure 6. The sea-surface heights (m) for the boreal summer over the entire model domain (A = 500 m^2 s^{-1}) without local wind forcing.

the x and y components of horizontal turbulent frictional force; and $\tau_x^{(b)}$ is the x component of bottom frictional force. Turbulent frictional forces and the bottom frictional force are divided by the mean density. It is worth noting that in the difference form we replace the integrals over S (in (28) and all the following integral relations) by the corresponding sums over those cells, where the x-momentum equation is used.

The notations below the separate terms in the equation relate to the column heading notations in Table 2. XCOR is the x-component of the Coriolis acceleration integrated over the total fluid volume, XPGRD is the x-component of the horizontal pressure gradient integrated over the same volume.

From Table 2 we see that basically XCOR is balanced by XPGRD, as expected from the

Table 2. The domain integral x-momentum balance terms for each season. Refer to text for the term definitions. The last column is explained in the next section.

Season (dimensions)	Coriolis (XCOR) 1×10^9 $\mathrm{m^4\ s^{-2}}$	Pressure gradient (XPGRD) 1×10^9 $\mathrm{m^4\ s^{-2}}$	Total pressure head (XPRH) 1×10^9 $\mathrm{m^4\ s^{-2}}$	External pressure head (XEPRH) 1×10^9 $\mathrm{m^4\ s^{-2}}$	Bottom form stress (XBTS) 1×10^9 $\mathrm{m^4\ s^{-2}}$	SSH difference (SSHDIF) 1×10^{-2} m
Winter	0.38×10^{-2}	0.10×10^{-1}	−0.30	−0.29	0.31	−0.96
Spring	−0.23	−0.23	−0.97	−0.96	0.74	−2.43
Summer	−0.45	−0.46	−1.65	−1.64	1.19	−3.97
Fall	−0.19	−0.19	−0.93	−0.92	0.74	−2.45

overall geostrophy of the motion in the region, except for the boreal winter when nonstationary terms in (28) appear significant. The integral advection of momentum, horizontal and bottom friction are insignificant. Recall that the effect of curvature of the coordinate system x, y (in other words, the variation of m_x and m_y) is very small. Otherwise the integral momentum balance would need to be considered in the vector form rather than in the component form.

The x-component of the resultant horizontal pressure gradient can be represented as:

$$\underbrace{-\int_S \frac{gD}{m_x}\frac{\partial\eta}{\partial x}\,dS}_{\text{XPGRD}} = \underbrace{-\int_S \frac{\partial}{m_x\partial x}(g\eta D)dS}_{\text{XPRH}} + \underbrace{\int_S \frac{g\eta}{m_x}\frac{\partial H}{\partial x}\,dS}_{\text{XBTS}} + \int_S \frac{g\eta}{m_x}\frac{\partial\eta}{\partial x}\,dS, \tag{30}$$

where XPRH is identified as the x-component of the resultant of pressure forces acting on the fluid at the side boundaries of the domain (both external and internal), and XBTS is identified as the x-component of the resultant of pressure forces acting on the fluid at the bottom, defined as the x-component of the bottom form stress (see Appendix B). The last term on the right-hand side of (30) is the x-component of the resultant of the pressure forces acting on the fluid at the free surface, which is negligible, as compared to XPRH or XBTS.

So far, we have used relatively loose terminology in describing the influence of the inter-ocean pressure difference. Now we will introduce the external pressure head, or simply "the pressure head," in the x-direction as:

$$\mathrm{XEPRH} = g\int_{\mathrm{south}}^{\mathrm{north}} [(D\eta)_{\mathrm{west}} - (D\eta)_{\mathrm{east}}]m_y dy, \tag{31}$$

where the integral is taken over the external western and eastern boundaries of the domain. In the difference form we used I = 6 for the western boundary and I = IM-5 for the eastern

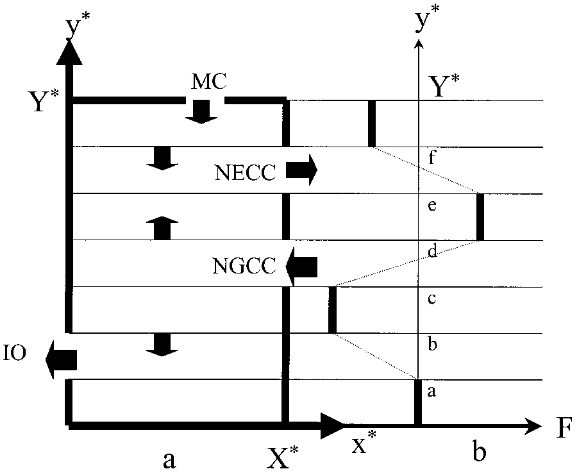

Figure 7. On the derivation of relation (34): Schematic of the total transports through the open ports IO, NGCC, NECC, MC and the sections $y^* = b$; d; f for the spring (a). Schematic of the graph of the function $F(y^*)$ for the spring: $F(b) = -Q_{\mathrm{IO}}$, $F(d) = -Q_{\mathrm{IO}} - Q_{\mathrm{NGCC}}$, $F(f) = Q_{\mathrm{MC}}$, see (27); (b). The dashed lines are linear interpolations.

boundary and excluded all land cells (see Fig. A.1). Then, the internal pressure head XIPRH is:

$$\mathrm{XIPRH} = \mathrm{XPRH} - \mathrm{XEPRH}. \tag{32}$$

The concept of the pressure head came from pipe or "simple channel" dynamics where the pressure head is defined as the net pressure force for two arbitrary cross-sections (in particular, for the entrance and exit region of the pipe or channel). This definition is appropriate in a dynamical sense because the pressure head terms appear in the integral momentum equations. So the approximate overall x-momentum equation is:

$$\mathrm{XCOR} = \mathrm{XEPRH} + \mathrm{XBTS} + \mathrm{XIPRH}. \tag{33}$$

As is seen from Table 2, XIPRH is negligibly small as compared to XEPRH for the case of real bottom topography.

XCOR can be expressed in terms of the total transport, Q_{IO}, along with transports through the MC, NECC, and NGCC open ports. To prove this we will introduce the coordinate system x^*, y^*, whose coordinate lines coincide with parallels and meridians, and corresponding velocity components U^* and V^*. The angle between x- and x^*-axes is approximately 17°. So we can assume that $V^* \cong V$. We calculate XCOR by integrating along $y^* =$ const (i.e., along parallels) taking into account that the Coriolis parameter, f, depends on latitude only. Then, $\mathrm{XCOR} = \int_0^{Y^*} f(y^*)F(y^*)m_{y^*}dy^*$, where $F(y^*) = \int_0^{X^*} VDm_{x^*}dx^*$' is the total transport through the section: $y^* =$ const. The schematic of the graph of $F = F(y^*)$ is given in Figure 7. We can consider m_{y^*} as a constant and,

Table 3. The domain integral y-momentum balance terms for each season. Refer to text for the term definitions. See also the explanation of terms in Part II, Appendix A.

Season (dimensions)	Coriolis (YCOR) 1×10^9 m^4 s^{-2}	Pressure gradient (YPGRD) 1×10^9 m^4 s^{-2}	Total pressure head (YPRH) 1×10^9 m^4 s^{-2}	External pressure head (YEPRH) 1×10^9 m^4 s^{-2}	Bottom form stress (YBTS) 1×10^9 m^4 s^{-2}
Winter	0.43	0.43	0.23	0.20	0.20
Spring	0.58	0.57	0.12	0.44×10^{-1}	0.45
Summer	0.75	0.74	0.42×10^{-1}	-0.81×10^{-1}	0.70
Fall	0.62	0.61	0.18	0.10	0.43

therefore, XCOR will be expressed as a linear combination of Q_{IO}, Q_{NGCC}, Q_{NECC}, Q_{MC}. Thus (33) can be rewritten as:

$$a_{\mathrm{IO}}Q_{\mathrm{IO}} + a_{\mathrm{NGCC}}Q_{\mathrm{NGCC}} + a_{\mathrm{NECC}}Q_{\mathrm{NECC}} + a_{\mathrm{MC}}Q_{\mathrm{MC}} = \mathrm{XEPRH} + \mathrm{XBTS} + \mathrm{XIPRH}, \qquad (34)$$

where coefficients a_{IO}, a_{NGCC}, a_{NECC}, and a_{MC} are easily calculated. We will not do such calculations and will restrict ourselves to the assertion that the relation between Q_{IO}, Q_{NGCC}, Q_{NECC}, Q_{MC}, XEPRH, XBTS, and XIPRH exist. Note that these coefficients do not depend on the bottom topography. Thus, the external pressure head XEPRH (or simply the pressure head) does not uniquely determine the ITF total transport (Q_{IO}). The bottom form stress XBTS plays a significant role in determining the transport Q_{IO} (see Table 2) along with the transports through MC, NECC, and NGCC ports. For the real bottom topography XIPRH is relatively small.

The expression for the integral y-momentum equation is analogous to (28):

$$\frac{\partial}{\partial t}\int_S VDdS + \int_S \left\{\frac{1}{m_x m_y}\left[\frac{\partial}{\partial x}(m_y UDV) + \frac{\partial}{\partial y}(m_x VDV)\right] + CUD\right\} dS$$
$$+ \underset{\text{YCOR}}{\int_S fUDdS} = \underset{\text{YPGRD}}{-\int_S \frac{gD}{m_y}\frac{\partial \eta}{\partial y}dS} + \int_S \{DF_y - \tau_y^{(b)}\}dS, \qquad (35)$$

with the notation located below separate terms of the equation related to Table 3 column headings and $\tau_y^{(b)}$ is the y component of the bottom frictional force. As in (28) we replace all integrals over S by the corresponding sums over those cells, where the y-momentum equation is used. Again, basically YCOR is balanced by YPGRD. The y-component of the integrated horizontal pressure gradient is written and interpreted similarly to (30):

$$\underset{\text{YPGRD}}{-\int_S \frac{gD}{m_y}\frac{\partial \eta}{\partial y}dS} = \underset{\text{YPRH}}{-\int_S \frac{\partial}{m_y \partial y}(g\eta D)dS} + \underset{\text{YBTS}}{\int_S \frac{g\eta}{m_y}\frac{\partial H}{\partial y}dS} + \int_S \frac{g\eta}{m_y}\frac{\partial \eta}{\partial y}dS. \qquad (36)$$

YEPRH and YIPRH are defined similarly to XEPRH and XIPRH (compare with (31) and (32)). So the external pressure head in the y-direction is:

$$\text{YEPRH} = g \int_{\text{west}}^{\text{east}} [(D\eta)_{\text{south}} - (D\eta)_{\text{north}}] m_x dx, \tag{37}$$

where the integral is taken over the external southern and northern boundaries of the domain. In the difference form we used J = 2 for the southern boundary and J = JM-5 for the northern boundary and excluded all land cells (see Fig. A.1). The internal pressure head in the y-direction is:

$$\text{YIPRH} = \text{YPRH} - \text{YEPRH}, \tag{38}$$

As is seen from Table 3 the y-component of the bottom form stress YBTS is significant. Note that in this case YIPRH is on the same order as YEPRH.

$$\text{YCOR} = \text{YEPRH} + \text{YIPRH} + \text{YBTS}. \tag{39}$$

It is not immediately clear how to express YCOR in terms of Q_{IO} and other transports.

The effect of bottom form stress on ocean dynamics is not new. Munk and Palmen (1951) were probably the first to draw attention to the importance of the bottom form stress for the dynamics of the Antarctic Circumpolar Current. Holland (1967; 1973) also discussed the importance of bottom form stress for boundary current dynamics. Our results provide strong evidence that the bottom form stress plays an important role in the Indonesian Seas dynamics. Preliminary results from our baroclinic model (15 sigma levels in the vertical, boreal summer case) also confirm that the bottom form stress is significant, even though the flow through parts of the Indonesian Sea is highly baroclinic (Burnett and Kamenkovich, 2002).

It is also worth noting that some estimates of the role of the curl of the bottom form stress (the bottom pressure torque) were reported by Schneider and Barnett (1997). We did not analyze the role of this term directly, so it is difficult to compare the results. In general, such comparisons are very difficult to perform because different models use different bottom topography. We are currently using accurate, unsmoothed bottom topography at a resolution of 1/12°. We did perform various sensitivity tests by changing the coefficient of horizontal turbulent friction from $A = 500 \text{ m}^2 \text{ s}^{-1}$ to $A = 50 \text{ m}^2 \text{ s}^{-1}$. In these cases the transport varied by 3–7% of their mean values similar to other modeling studies performed by Inoue and Welsh (1993), Lebedev and Yaremchuck (2000); and Potemra (1999). These tests validate our observation that horizontal friction is insignificant over the model domain.

We will now analyze the overall energy balances. The integral energy equation is written as follows (see Appendix C for a detailed explanation):

Table 4. The domain integral energy balance terms for each season experiments with $A = 500\ \text{m}^2\ \text{s}^{-1}$ and no wind stress. Refer to text for the term definitions.

Season (dimensions)	(−) Work of pressure forces (PREWK) $1 \times 10^6\ \text{m}^5\ \text{s}^{-3}$	Work of horizontal friction (HFWK) $1 \times 10^6\ \text{m}^5\ \text{s}^{-3}$	Work of bottom friction (BFWK) $1 \times 10^6\ \text{m}^5\ \text{s}^{-3}$
Winter	−0.76	−0.72	-0.66×10^{-1}
Spring	−2.39	−1.88	−0.35
Summer	−5.65	−4.14	−1.19
Fall	−2.49	−2.13	−0.41

$$\frac{\partial}{\partial t}\int_S \left(D\frac{U^2+V^2}{2} + g\frac{\eta^2}{2}\right)dS + \oint_\Gamma D\left(\frac{U^2+V^2}{2}\right)(\mathbf{U}\cdot\mathbf{n})d\Gamma$$

$$+ \underbrace{\oint_\Gamma g\eta D(\mathbf{U}\cdot\mathbf{n})d\Gamma}_{\text{PREWK}} = \underbrace{-\int_S (\tau_x^{(b)}U + \tau_y^{(b)}V)dS}_{\text{BFWK}} + \underbrace{\int_S (DF_xU + DF_yV)dS}_{\text{HFWK}}, \tag{40}$$

where Γ is the contour bounding the area, S, and some notations are located below the separate terms of this equation. The integration over Γ is taken only across the four open ports. PREWK (opposite in sign) is the total work performed by pressure forces at the four ports, BFWK is the total work preformed by bottom friction over the model domain, and HFWK is the total work performed by horizontal friction over the fluid volume (all per unit time). As in (28) and (35) we replace all integrals by the corresponding sums.

Table 4 shows the integral energy balance terms for each season. Similar to the integral momentum balances, the change in the total energy with time can be neglected. The advection of the kinetic energy is also small compared to other terms in the equation. Except for the winter season, the work performed by the pressure forces at the ports (-PREWK) is practically balanced by the sum of the work of horizontal frictional forces (HFWK) over the fluid volume and the work of bottom frictional forces (BFWK) over the model domain, for each season. When $A = 500\ \text{m}^2\ \text{s}^{-1}$ the work of horizontal friction is larger than the work of bottom friction, but reducing $A = 50\ \text{m}^2\ \text{s}^{-1}$ decreases the work of horizontal friction, making it comparable with the work of bottom friction. In the winter, the PREWK term is basically balanced by the HFWK term.

In contrast with the pipe dynamics, the analysis of the energy balance, generally speaking, does not necessarily lead to an estimate of the role of the pressure head (see note at the end of Section 2). But if we replace η by a mean value, η_P, in the Pacific Ocean part of the domain and correspondingly by a mean value, η_I, in the Indian Ocean part, then the negative of the work performed by pressure forces per unit time will be

$$\text{PREWK} = g\eta_P(Q_{MC} + Q_{NECC} + Q_{NGCC}) + g\eta_I Q_{IO} = g(\eta_I - \eta_P)Q_{IO}, \tag{41}$$

where (27) was used. Now PREWK can be used as a proxy to measure the pressure head across the model domain. In our experiments PREWK is small in the winter and substantially larger in the summer (Table 4).

Wyrtki (1987) used sea level data from Davao, Philippines and Darwin, Australia to determine the annual and the interannual variations of the ITF. Inoue and Welsh (1993), Potemra *et al.* (1997), and Lebedev and Yaremchuk (2000) also used a similar approach to determine the variation of the total transport of the ITF. Similar to their techniques, we can measure the pressure head by analyzing the difference of surface heights at some fixed locations in the Indian Ocean and in the Pacific. The western side at the mouth of the MC open port (I = 166, J = 246) is used as the Pacific location, since it is in close approximation to Wyrtki's Davao, Philippines site. However, the northern side at the mouth of the IO open port (I = 5, J = 49) was chosen as the Indian Ocean location, away from the Darwin, Australia site. The IO port was selected since the largest sea-surface height differences in the model are between the Pacific Ocean MC port and the Indian Ocean IO port. In Table 2, these values are denoted SSHDIF as another proxy to measure the pressure head between the Pacific and Indian Ocean. Similar to XEPRH and PREWK, SSHDIF is small in the winter and larger in the summer.

In another experiment we ran the model with a boreal spring transport and set the bathymetry to a constant depth, throughout the model domain, at $H = 4500$ m, to eliminate the effect of bottom form stress. Wind stress was not incorporated into this model. The horizontal velocity pattern (Fig. 8) indicates that the majority of the transport follows the western boundary of the model domain, with the flow traveling from the Celebes Sea southern coast, through the Makassar and Lombok Straits, and exiting through the IO. There is very little transport through the major passageways of the Ombai Strait and the Timor Sea. The flow from the NGCC enters the Halmahera Sea, rotates anticyclonically around the Molucca Sea, and returns to the Pacific Ocean.

An analysis of the integral momentum equations for the case where $H =$ const. indicates that:

$$\mathrm{XCOR} = \mathrm{XEPRH} + \mathrm{XIPRH}, \quad \mathrm{YCOR} = \mathrm{YEPRH} + \mathrm{YIPRH}. \tag{42}$$

Notice that now XBTS and YBTS are equal to zero. In this experiment, XCOR changed by only 17% (YCOR changed by 36%) as compared to the real bottom topography experiment. This supports the relation (34) according to which XCOR depends linearly on transports through the ports (Q_{IO}, Q_{MC}, Q_{NECC}, Q_{NGCC}) and that the corresponding coefficients (a_{IO}, a_{NGCC}, a_{NECC}, and a_{MC}) do not depend on the bottom topography. Note that XEPRH $= 0.20 \times 10^9$ m^4 s^{-2} and YEPRH $= 0.37 \times 10^9$ m^4 s^{-2} for $H =$ const. Thus, XEPRH and YEPRH substantially change compared to the corresponding values for the real bottom topography (80% and 90%, respectively) and that XIPRH and YIPRH basically balance these changes correspondingly. Because the total transport of the ITF is the same in both the real bottom topography and $H =$ const. cases, this observation

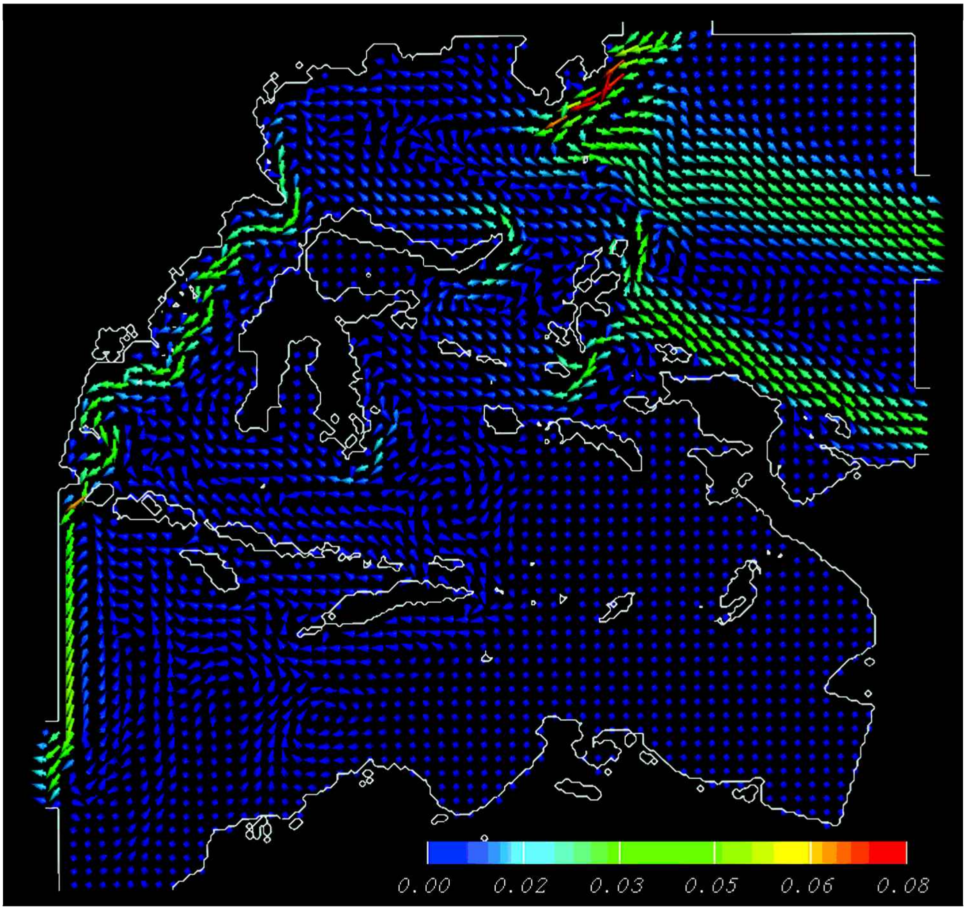

Figure 8. The horizontal velocity pattern (m s^{-1}) for $H = 4500$ m, without local wind forcing.

provides additional evidence that the total transport of the ITF and the pressure head are not uniquely related. Thus, when $H =$ const. the bottom form stresses, XBTS and YBTS, are zero and the internal pressure head, XIPRH, equaled the external pressure head, XEPRH. The same is true for YIPRH.

We conclude with an analysis of the integral momentum balances for flows with local wind forcing but with the same port transport values. In this case we use the terms $\int_S \tau_x dS$ and $\int_S \tau_y dS$ on the right-hand side of (28) and (35). The wind stress term (WUSURF) is on the same order of magnitude as XCOR and XPGRD, and bottom friction is increased and now comparable with the XCOR term as well. The advection of momentum, the horizontal diffusion of momentum, and nonstationary terms remain negligible. XCOR did not change substantially except in the winter. We observed rather strong changes in XEPRH (except in the fall) that supports our point that the total transport of the ITF depends not only on the pressure head, but also on the wind stress and other factors. It is worth mentioning that the bottom form stress, XBTS, changed substantially between the northwest and southwest monsoon, along with the XIPRH. Approximately the same conclusions are true for the analysis of integral y-momentum equation.

7. Conclusions

To study the influence of the Pacific-Indian Ocean pressure difference on the total transport of the Indonesian Throughflow (ITF) two models have been considered. The first-step heuristic channel model is used to derive simple analytic relations between the pressure gradient along the channel and the total transport of the channel flow for several hypothetical flows. The analysis suggests that the bottom relief and local winds can substantially influence such relations. To further our analysis, we developed a second-step model that is a regional barotropic model based on the Princeton Ocean Model. A realistic bottom topography and coastline was incorporated into this model. Four open ports simulate the major ocean currents that influence the ITF: the Mindanao Current (MC) inflow, the North Equatorial Counter Current (NECC) outflow, the New Guinea Coastal Current (NGCC) inflow, and the Indian Ocean (IO) outflow. A series of numerical experiments with prescribed seasonally varying transports were performed and the overall momentum and energy balances of the ensuing flow patterns have been studied.

Our comparison of the model horizontal circulation patterns and transports with observations and other modeling studies verify that the regional barotropic model with prescribed seasonally varying port transports is able, in general, to reproduce the main features of the Indonesian Seas circulation. Sea-surface height patterns indicate that the model develops higher sea-surface heights in the Pacific Ocean domain and lower elevations in the Indian Ocean domain, in general compliance with observations. It is shown that the model always develops a seasonally varying pressure head that accompanies the ITF.

An investigation of the overall balance of momentum and energy shows that the volume integral of the Coriolis acceleration essentially balances the volume integral of the pressure gradient plus the domain integral of the wind stress. The contributions from the volume integral of the horizontal diffusion of momentum and momentum advection are small. The bottom friction is typically small but in some experiments with local wind forcing it became comparable with the volume integral of the Coriolis acceleration. This result indicates that without local wind forcing the geostrophic approximation can be accepted for a majority of the Indonesian Seas area. The areas where geostrophy may not pertain have been described in Burnett *et al.* (2000a). If the local winds are incorporated, the overall geostrophic balance is influenced by the wind effect. The volume integrals of separate terms of the energy equation were also calculated, and the results show that the work of the pressure force at the open ports (per unit time) is balanced by the work of horizontal frictional force and the work of bottom friction over the model domain (per unit time). The advection of kinetic energy through the open ports is small.

Special tools have been developed to interpret the results of the numerical experiments. They are, for example, the external and internal pressure heads, the bottom form stress, and the interpretation of the domain integral of the x-component of the Coriolis acceleration, see (34). We would like to mention two additional characteristics (proxies) to quantitatively measure the pressure head between the Pacific and Indian Ocean. They are the total work performed by pressure forces (per unit time) at the four open ports of the model and the surface height difference at fixed locations within the Pacific and Indian Ocean. Wyrtki (1987) originally suggested the latter approach. The proxies were tested for each season: during the southeast monsoon (boreal summer) the pressure head was larger when the prescribed transport was higher, and during the northwest monsoon (boreal winter) the pressure head was reduced when the prescribed transport was at a minimum.

The analysis of various experiments (with realistic bottom topography and with a constant depth; with local wind forcing and without local wind forcing) provided strong evidence that the value of the total transport depends not only on the Pacific-Indian Ocean pressure head and local winds but on other factors as well. One factor is the bottom topography—more precisely the bottom form stress. Another factor is the internal pressure head, which is caused by the action of pressure on the sidewalls of islands and internal portions of land. An additional factor is the total inflow and outflow transports caused by the Mindanao Current, North Equatorial Counter Current, and New Guinea Coastal Current (see the approximate relation (34)). We stress that several experiments performed with the same total transport but with different bottom topography provided substantially different values of the pressure head. Thus it appears that the two external driving factors (the pressure head and local winds) do not uniquely determine the total transport of the ITF.

In Part II of our study (Kamenkovich *et al.,* 2003) we will perform additional experiments with the barotropic model to prove the robustness of our main result on the lack of the unique relation between the pressure head and the total transport (more precisely the robustness of the relation (34)). Yet, we will show that seasonal variations of the total transport are in-phase with those of different measures of the pressure head.

Acknowledgments. First of all, we would like to thank George Veronis for a very productive discussion that resulted in the considerable clarification of several points of the paper, especially in Section 2. The authors gratefully acknowledge helpful advice from H. Hurlburt and D. Nechaev on different aspects of the paper. We are also grateful to K. Lebedev and M. Yaremchuk for providing us with the results of their diagnostic calculations. The criticism of our three reviewers was very useful and allowed us to substantially modify the initial outline of the material. W. Burnett was supported by U.S. Navy funds. V. Kamenkovich was supported by the NSF grants OCE 96-33470 and OCE 01-18200. A. Gordon was supported by NSF grants OCE 00-99152 and OCE 96-33470. G. Mellor was supported by NSF grant OCE 96-33470. The model analysis was supported by the Department of Defense's Major Shared Resource Center. The Naval Oceanographic Office Visualization Laboratory prepared the color graphics.

APPENDIX A

Difference formulation

Figure A.1 presents a schematic of the grid configuration, which consists of 250 × 250 cells at approximately 10 km resolution, as well as the names and locations of the four open ports (refer also to Table A.1). Each cell is identified by two numbers (I, J): I = 1, . . . , 250; J = 1, . . . , 250. The grid resolution is sufficient to adequately resolve the major passageways (Table A.2). The open ports are modeled as a channel with a length of five grid cells. This computational device allows us to weaken or suppress numerical noise due to the prescribed open boundary conditions. Physical interpretations from the numerical experiments were done within the operational domain: I = 5, . . . , 246; J = 2, . . . , 246.

Grid cells are identified as land cells if the cell depth, $H(\mathrm{I}, \mathrm{J}) < H_{\min}$, and $H_{\min} = 10$ m. We treat the external boundary cells of the model domain as land cells, except at the open ports, to control the inflow and outflow. The cells corresponding to the Sunda Shelf/Java Sea are treated as land cells based on bathymetric charts that indicate the choke point between the Sunda Shelf and the Java Sea at the Karimata Strait is only 1/6° wide at the 30-m isobath and only 29 m deep at sill depth. It is based also on results from the Metzger and Hurlburt (1996) 1/2°, 1.5-layer global reduced gravity thermodynamic model showing the Java Sea did not significantly affect the ITF. The Torres Strait is closed based on results by Gordon and McClean (1999), analyzing an eddy-resolving, 20-level, primitive equation

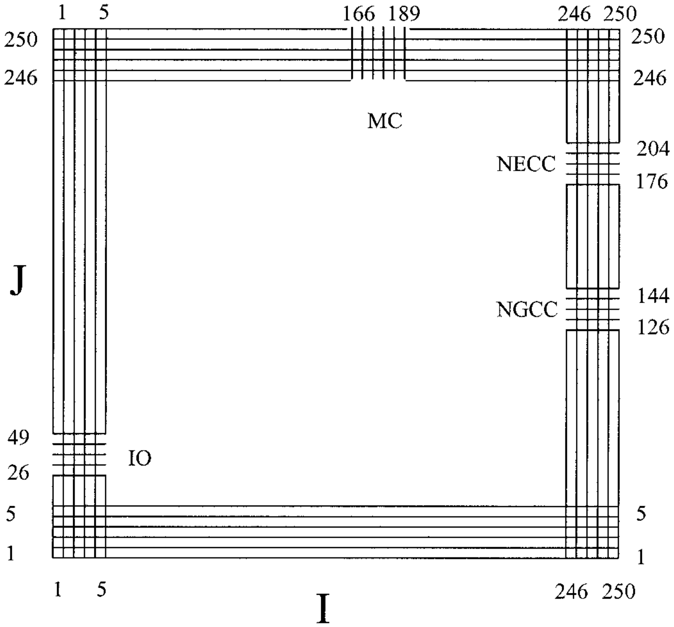

Figure A.1. Schematic of the 250 × 250 model domain and the locations of the four open ports. The channel lengths are five grid cells.

Table A.1. Locations of the 4 open ports within the model domain and their prescribed transports.

Ports	Transports (Sv)	Locations
Mindanao Current (inflow)	Winter: −20.5 Spring: −22.0 Summer: −26.0 Fall: −27.0	$166 \leq I \leq 189$ $246 \leq J \leq 250$
Indian Ocean Current (outflow)	Winter: 5.0 Spring: 12.5 Summer: 20.0 Fall: 12.5	$1 \leq I \leq 5$ $26 \leq J \leq 49$
New Guinea Coastal Current (inflow)	Winter: −14.0 Spring: −16.5 Summer: −19.0 Fall: −16.5	$246 \leq I \leq 250$ $126 \leq J \leq 144$
North Equatorial Counter Current (outflow)	Winter: 29.5 Spring: 26.0 Summer: 25.0 Fall: 31.0	$246 \leq I \leq 250$ $176 \leq J \leq 204$

global model forced by ECMWF wind stress. They showed that closing the Torres Strait, with a total effective cross-section area that does not exceed 0.2 km^2, leads to a realistic throughflow configuration. Note that following the usual approach the Sulu Sea is closed to reduce the number of open ports in this experiment. However some studies, Metzger and Hurlburt (1996) and Lebedev and Yaremchuk (2000), indicate that the flow through the Sulu archipelago might influence the ITF.

For a single grid cell molecule, $U(\mathrm{I}, \mathrm{J})$ is defined at the center of the left side of a grid cell;

Table A.2. The grid cell width of the 4 open ports and 8 major passageways. The letters next to the names of the passageways are used to identify the locations of the passageway cross-sections in Figure 1.

Passage	Width (number of grid cells)
IO outflow	24
NGCC inflow	19
NECC outflow	29
MC inflow	24
Makassar Strait (A)	25
Molucca Sea (B)	44
Halmahera Sea (C)	19
Lombok Strait (D)	5
Sumba Strait (E)	7
Flores Sea (F)	26
Ombai Strait (G)	14
Timor Sea (H)	62

V(I, J) at the center of the bottom side of a grid cell; and η(I, J) at the center of a grid cell (the C-grid configuration). To formulate the corresponding difference equations, the basic equations are integrated over each interior grid cell using a time discretization based on the leap-frog scheme. The difference scheme is explicit. To calculate U, V, and η at the next time step, first use the difference forms of the basic equations to determine U, V, and η at all grid points, apply the boundary conditions, and then set U, V and η to zero (masking) at the land cells.

The description of the open port boundary conditions is based on the IO open port (I $=$ 1, . . . , 5; 26 $\leq$ J $\leq$ 49); however, other ports are handled similarly. Normal velocities are prescribed at I $=$ 2, U(2, J); the tangential velocities are prescribed at I $=$ 1, V(1, J) $=$ 0; and the computational boundary condition are η(1, J) $=$ η(2, J), and U(1, J) $=$ U(2, J). A schematic is provided in Figure A.2.

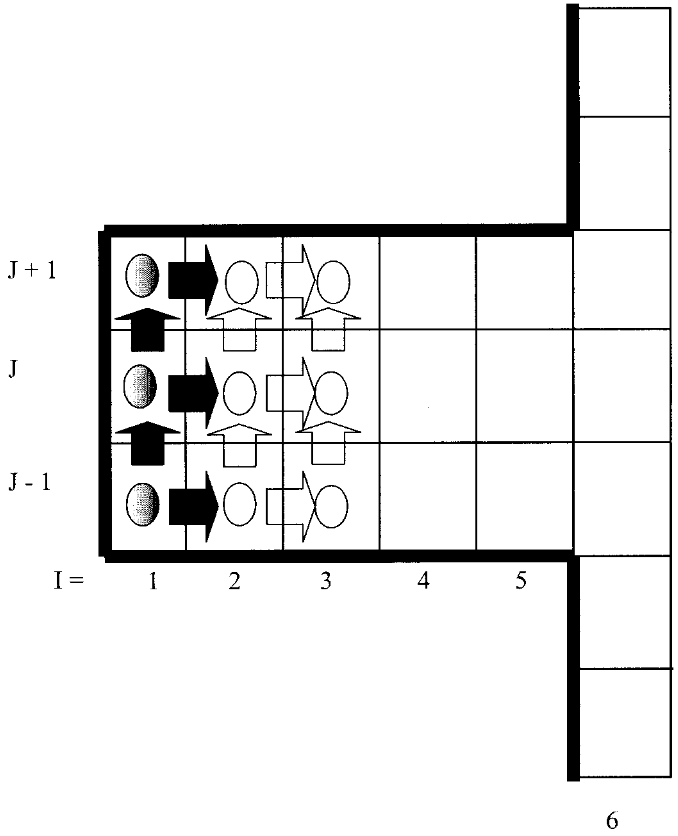

Figure A.2. The schematic of the specified and calculated U, V, and η for the IO port (26 $\leq$ J $\leq$ 49) for I $=$ 1; 2; 3. The prescribed normal, U(2, J), and tangential velocities V(1, J) are denoted by black arrows; the computational boundary conditions are η(1, J) $=$ η(2, J) (denoted by partially filled ovals) and U(1, J) $=$ U(2, J) (not shown). Clear arrows and ovals denote variables that are calculated by using dynamical equations.

The topography is ETOPO5 bathymetry at 1/12° resolution (see Fig. 2); monthly wind stresses are derived from Hellerman and Rosenstein (1983) at 2° latitude by 2° longitude resolution; the time step is 14 seconds; and the coefficient of horizontal friction is $A = 500\ \mathrm{m}^2\,\mathrm{s}^{-1}$ (or $50\ \mathrm{m}^2\,\mathrm{s}^{-1}$ for sensitivity experiments).

APPENDIX B

Interpretation of the pressure force terms in Eqs. (30) and (36)

The pressure, p, can be represented as $p = p_a - g\rho_o(z - \eta)$, where p_a is the constant atmospheric pressure; ρ_o is the mean density. The resultant of the pressure forces acting on the volume, V, bounded by the surface, Σ, is equal to $-\oint_\Sigma p\mathbf{n}d\Sigma$, where $\mathbf{n}$ is the unit outward normal with regards to the surface Σ. According to the divergence theorem this term is equal to $-\int_V \nabla p dV$. Therefore, only the deviation from the hydrostatic pressure (the perturbation of pressure), $g\rho_o\eta$, contributes to the horizontal components of the resultant pressure force.

Figure B.1 presents a schematic of the x-component of the bottom form stress (XBTS) and the pressure forces acting at the side boundaries (XEPRH and XIPRH). To calculate the x- and y-components of the resultant of pressure forces acting on the bottom, we use the following formula for the x- and y-components of the unit outward normal:

$$(n_x, n_y) = -\left(\frac{\partial H}{m_x \partial x}; \frac{\partial H}{m_y \partial y}\right) \Big/ \sqrt{1 + \left(\frac{\partial H}{m_x \partial x}\right)^2 + \left(\frac{\partial H}{m_y \partial y}\right)^2} \tag{B.1}$$

and the area element of the surface, $z = -H(x, y)$ is:

$$d\Sigma = \sqrt{1 + \left(\frac{\partial H}{m_x \partial x}\right)^2 + \left(\frac{\partial H}{m_y \partial y}\right)^2}\, dS. \tag{B.2}$$

Thus, the sought x- and y-components of the force per unit mass are:

$$\frac{1}{\rho_o}\int_\Sigma p n_x d\Sigma = \int_S g\eta \frac{\partial H}{m_x \partial x} dS; \qquad \frac{1}{\rho_o}\int_\Sigma p n_y d\Sigma = \int_S g\eta \frac{\partial H}{m_y \partial y} dS \tag{B.3}$$

respectively.

For difference forms of (28), (35), and (40) we used the difference forms of the corresponding momentum and energy equations and replaced all the integrals by the sum over those grid points for which the x-momentum (or y-momentum) equations are written. The same summing should be used for (31) and (37).

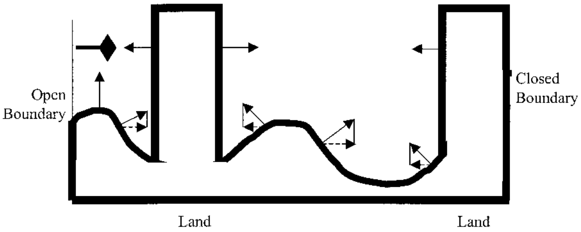

Figure B.1. Schematic of a section of the fluid volume ($y = const$). Shown are the x-components of the pressure forces acting on the fluid at the side boundaries of the domain, and the x-components of pressure forces acting on the fluid at the bottom. The sum of all the diamond arrows gives the external side boundary action or the pressure head (XEPRH); the sum of all the normal arrows gives the internal side boundary action or the internal pressure head (XIPRH). The resultant of all the pressure forces acting on the fluid at the bottom gives the bottom form stress.

APPENDIX C

Interpretation of the pressure work term in Eq. (40)

The sum of the work (per unit time) performed by the gravity force and the external pressure forces is given by:

$$A = \int_S \left[-\int_{-H}^{\eta} g\rho_o W dz \right] dS + \int_\Gamma \left[-\int_{-H}^{\eta} (p\mathbf{n} \cdot \mathbf{U}) dz \right] d\Gamma \tag{C.1}$$

where W is the vertical velocity and Γ is the contour bounding the area S. The second term on the right-hand side of (C.l) gives the work (per unit time) performed at the side-walls of the domain. The work of the pressure forces acting on the bottom is equal to zero ($\mathbf{U} \cdot \mathbf{n} = 0$). Since the pressure at the free surface, p_a, is constant, the work of pressure forces at this surface is: $-p_a \int_S (\mathbf{U} \cdot \mathbf{n}) dS$ and, according to mass conservation, this term is also equal to zero.

Taking into account that the horizontal velocities do not depend on z:

$$W = \frac{z - \eta}{D} \frac{dH}{dt} + \frac{z + H}{D} \frac{d\eta}{dt} \tag{C.2}$$

where d/dt is the material time derivative. After some manipulations:

$$-\int_{-H}^{\eta} gW dz = -g \frac{\partial}{\partial t}\left(\frac{\eta^2}{2}\right) + \frac{g}{2} \nabla \cdot [D(H - \eta)\mathbf{U}] \tag{C.3}$$

Further:

$$-\frac{1}{\rho_o} \int_{-H}^{\eta} p(\mathbf{n} \cdot \mathbf{U}) dz = -(\mathbf{U} \cdot \mathbf{n}) \frac{gD^2}{2}. \tag{C.4}$$

Thus, applying the divergence theorem to the second term on the right-hand side of (C.4) and using the relation $D(H - \eta) - D^2 = -2D\eta$ gives:

$$A = \int_S \left[-g\rho_o \frac{\partial}{\partial t}\left(\frac{\eta^2}{2}\right) - g\rho_o \nabla \cdot (D\eta\mathbf{U}) \right] dS. \tag{C.5}$$

The second term on the right-hand side of (C.5) can be recognized as the work (per unit time) performed by the perturbation of pressure at the side boundaries of the domain [refer to (40)].

REFERENCES

Arief, D. and S. P. Murray. 1996. Low-frequency fluctuations in the Indonesian throughflow through Lombok Strait. J. Geophys. Res., *101*(C5), 12,455–12,464.

Blumberg, A. F. and G. L. Mellor. 1987. A description of a three-dimensional coastal ocean circulation model. Three-Dimensional Coastal Ocean Models, *4,* N. Heaps, ed., Amer. Geophys. Union, Washington, DC, 208 pp.

Burnett, W. H. 2000. A dynamical analysis of the Indonesian Seas Throughflow. Ph.D. dissertation, Department of Marine Science, University of Southern Mississippi, Hattiesburg, MS, 114 pp.

Burnett, W. H. and V. M. Kamenkovich. 1999. The influence of the pressure head on the Indonesian Seas circulation. Third Conference on Coastal Atmospheric and Oceanic Prediction and Processes; 3–5 November 1999; New Orleans, LA. Amer. Meteor. Soc., 385–388.

—— 2002. On the splitting of main currents on the Indonesian Seas. Oceans 2002 Conference; 29–31 October 2002; Biloxi, MS, Marine Technology Society.

Burnett, W. H., V. M. Kamenkovich, D. A. Jaffe, A. L. Gordon and G. L. Mellor. 2000a. Dynamical balance in the Indonesian Seas circulation. Geophys. Res. Lett., *27,* 2,705–2,708.

Burnett, W. H., V. M. Kamenkovich, G. L. Mellor and A. L. Gordon. 2000b. The influence of the pressure head on the Indonesian Seas circulation. Geophys. Res. Lett., *27,* 2,273–2,276.

Chong, J. C., J. Sprintall, S. Hautala, W. Morawitz, N. A. Bray and W. Pandoe. 2000. Shallow throughflow variability in the outflow straits of Indonesia. Geophys. Res. Lett., *27,* 125–128.

Ffield, A. and A. L. Gordon. 1992. Vertical mixing in the Indonesian thermocline. J. Phys. Oceanogr., *22,* 184–195.

Fieux, M., R. Molcard and A. G. Ilahude. 1996. Geostrophic transport of the Pacific-Indian Oceans throughflow. J. Geophys. Res., *101*(C5), 12,421–12,432.

Fine, R. A. 1985. Direct evidence using tritium data for throughflow from the Pacific into the Indian Ocean. Nature, *315,* 478–480.

Fine, R., R. Lukas, F. M. Bingham, M. J. Warner and R. H. Gammon. 1994. The western equatorial Pacific: A water mass crossroads. J. Geophys. Res., *99,* 25,063–25,080.

Godfrey, J. S. 1989. A Sverdrup model of the depth-integrated flow for the World Ocean, allowing for island circulations. Geophys. Astrophys. Fluid Dyn., *45,* 89–112.

—— 1996. The effect of the Indonesian throughflow on ocean circulation and heat exchange with the atmosphere: A review. J. Geophys. Res., *101*(C5), 12,217–12,237.

Godfrey, J. S. and Y. Masumoto. 1999. Diagnosing the mean strength of the Indonesian throughflow in an ocean general circulation model. J. Geophys. Res., *104*(C4), 7889–7895.

Gordon, A. L. 1986. Interocean exchange of thermocline water. J. Geophys. Res., *91,* 5,037–5,046.

—— 2001. Interocean exchange, Chapter 4.7 *in* Ocean Circulation and Climate, G. Siedler, J. Church, and J. Gould, eds., Academic Press, 303–314.

Gordon, A. L. and R. A. Fine. 1996. Pathways of water between the Pacific and Indian oceans in the Indonesian Seas. Nature, *379,* 146–149.

Gordon, A. L. and J. L. McClean. 1999. Thermohaline stratification of the Indonesian Seas: Modeling and observations. J. Phys. Oceanogr., *29,* 198–216.

Gordon, A. L., R. D. Susanto and A. L. Ffield. 1999. Throughflow within Makassar Strait. Geophys. Res. Lett., *26,* 3325–3328.

Hellerman, S. and M. Rosenstein. 1983. Normal monthly wind stress over the world ocean with error estimates. J. Phys. Oceanogr., *13,* 1,093–1,104.

Holland, W. R. 1967. On the wind-driven circulation in an ocean with bottom topography. Tellus, *19,* 582–599.

—— 1973. Baroclinic and topographic influences on the transport in western boundary currents. Geophys. Fluid Dyn., *4,* 187–210.

Inoue, M. and S. E. Welsh. 1993. Modeling seasonal variability in the wind-driven upper-layer circulation in the Indo-Pacific region. J. Phys. Oceanogr., *23,* 1,411–1,436.

Kamenkovich, V. M., W. H. Burnett, A. L. Gordon and G. L. Mellor. 2003. The Pacific/Indian Ocean pressure difference and its influence on the Indonesian Seas circulation: Part II—The study with specified sea-surface heights. J. Mar. Res., *61,* 613–634.

Kashino, Y., E. Firing, P. Hacker, A. Sulaiman and Lukiyanto. 2001. Currents in the Celebes and Maluku Seas. Geophys. Res. Lett., *28,* 1,263–1,266.

Kindle, J. C., G. W. Heburn and R. C. Rhodes. 1987. An estimate of the Pacific to Indian Ocean throughflow from a global numerical model, *in* Further Progress in Equatorial Oceanography, E. J. Katz and J. M. Witte, eds., Nova University Press, 317–321.

Kindle, J. C., H. E. Hurlburt and E. J. Metzger. 1989. On the seasonal and interannual variability of the Pacific to Indian Ocean throughflow, *in* Proceedings of the Western Pacific International Meeting and Workshop on TOGA COARE, J. Picaut, R. Lukas and T. Delcroix, eds., Inst. Fr. De Rech. Sci. pour le Dev. En Coop. (ORSTOM), Noumea, New Caledonia, 355–365.

Lebedev, K. V. and M. I. Yaremchuk. 2000. A diagnostic study of the Indonesian throughflow. J. Geophys. Res., *105*(C5), 11,243–11,258.

Lighthill, J. 1996. An Informal Introduction to Theoretical Fluid Mechanics, The Institute of Mathematics and its Applications. Clarendon Press, Oxford, 260 pp.

Lukas, R., T. Yamagata and J. P. McCreary. 1996. Pacific low-latitude western boundary currents and the Indonesian throughflow. J. Geophys. Res., *101*(C5), 12,209–12,216.

Mellor, G. L. 1999. Users guide for a three-dimensional, primitive equation, numerical ocean model. Princeton University, Princeton, NJ, 40 pp.

Metzger, E. J. and H. E. Hurlburt. 1996. Coupled dynamics of the South China Sea, the Sulu Sea, and the Pacific Ocean. J. Geophys. Res., *101*(C5), 12,331–12,352.

Miyama, T., T. Awaji, K. Akitomo and N. Imasato. 1995. Study of seasonal transport variations in the Indonesian Seas. J. Geophys. Res., *100*(C10), 20,517–20,541.

Murray, S. P. and D. Arief. 1988. Throughflow into the Indian Ocean through the Lombok Strait, January 1985–January 1986. Nature, *333,* 444–447.

Murray, S. P., E. Lindstrom, J. Kindle and E. Weeks. 1995. Transport through the Vitiaz Strait, WOCE Notes, *7,* 21–23.

Munk, W. H. 1950. On the wind-driven ocean circulation. J. Meteorol., *7,* 79–93.

Munk, W. H. and E. Palmen. 1951. Note on the dynamics of the Antarctic Circumpolar Current. Tellus, *3,* 53–55.

Nof, D. 1995a. Choked flows and wind-driven interbasin exchange. J. Mar. Res., *53,* 23–48.

—— 1995b. Choked flows from the Pacific to the Indian Ocean. J. Phys. Oceanogr., *25,* 1,369–1,383.

—— 1996. What controls the origin of the Indonesian throughflow? J. Geophys. Res., *101*(C5), 12,301–12,314.

Potemra, J. T., R. Lukas and G. T. Mitchum. 1997. Large-scale estimation of transport from the Pacific to the Indian Ocean. J. Geophys. Res., *102*(C13), 27,795–27,812.

Potemra, J. T., S. L. Hautala, J. Sprintall and W. Pandoe. 2002. Interaction between the Indonesian Seas and the Indian Ocean in observations and numerical models. J. Phys. Oceanogr., *32,* 1838–1854.

Pratt, L. J. 1991. Geostrophic versus critical control in straits. J. Phys. Oceanogr., *21,* 728–732.

Qiu, B., M. Mao and Y. Kashino. 1999. Intraseasonal variability in the Indo-Pacific throughflow and the regions surrounding the Indonesian Seas. J. Phys. Oceanogr., *29,* 1,599–1,618.

Schneider, N. and J. P. Barnett. 1997. Indonesian throughflow in a coupled general circulation model. J. Geophys. Res., *102*(C6), 12,341–12,358.

Stommel, H. and A. B. Arons. 1960. On the abyssal circulation of the world ocean—I. Stationary planetary flow patterns on a sphere. Deep-Sea Res., *6,* 140–154.

Toulany, B. and C. Garrett. 1984. Geostrophic control of fluctuating barotropic flow through straits. J. Phys. Oceanogr., *14,* 649–655.

Veronis, G. 1981. Dynamics of large-scale ocean circulation, *in* Evolution of Physical Oceanography. Scientific Surveys in Honor of Henry Stommel, B. A. Warren and Carl Wunsch, eds., The MIT Press, Cambridge, MA and London, England, 140–183.

Wajsowicz, R. C. 1993a. The circulation of the depth-integrated flow around an island with application to the Indonesian throughflow. J. Phys. Oceanogr., *23,* 1470–1484.

—— 1993b. A simple model of the Indonesian throughflow and its composition. J. Phys. Oceanogr., *23,* 2683–2703.

—— 1994. A relationship between interannual variations in the South Pacific wind stress curl, the Indonesian throughflow, and the West Pacific warm water pool. J. Phys. Oceanogr., *24,* 180–2,187.

—— 1999. Models of the Southeast Asian Seas. J. Phys. Oceanogr., *29,* 986–1,018.

Wyrtki, K. 1961. Physical oceanography of the southeast Asian waters. Scientific results of marine investigations of the South China Sea and Gulf of Thailand 1959–1961. NAGA Rep. 2, Scripps Inst. Oceanogr., La Jolla, CA., 195 pp.

—— 1987. Indonesian throughflow and the associated pressure gradient. J. Geophys. Res., *92*(C12), 12,941–12,946.

Received: *21 August, 2001;* revised: *9 September, 2003.*